Residual stress and adhesion of thermal spray coatings: microscopic view by solidification and crystallisation analysis in the epitaxial CoNiCrAlY single splat

F. Fanicchia[a,b], X. Maeder[a], J. Ast[a], A. A. Taylor[a], Y. Guo[a], M. N. Polyakov[a], J. Michler[a], D. Axinte[b,*]

[a]*Empa, Swiss Federal Laboratories for Materials Testing and Research, Laboratory for Mechanics of Materials and Nanostructures, Feuerwerkerstrasse 39, CH-3602 Thun, Switzerland*
[b]*Rolls-Royce UTC in Manufacturing and On-Wing Technology, Faculty of Engineering, University of Nottingham, NG7 2RD, UK*

Abstract

A new approach is proposed to achieve an in-depth understanding of crystallisation, residual stress and adhesion in epitaxial splats obtained by Combustion Flame Spray. Modelling of the fundamental process mechanisms is achieved with the help of experimental observations providing details with a sub-micrometre spatial resolution. At this scope, High Angular Resolution Electron Backscatter Diffraction and Transmission Electron Microscopy analysis are employed to provide insights into crystallisation and residual stress levels, while FIB-milled microcantilever beam bending is used for fracture strength measurements in the case of single splats. A comparison to fully-developed coatings is achieved by employing the X-ray Diffraction $sin^2\psi$ technique and pull-off methods for residual stress and fracture strength, respectively. The methodology is applied to metallic CoNiCrAlY material sprayed onto a Ni-based superalloy substrate. The establishment of different crystallisation regions: epitaxial and polycrystalline, is the result of variations in the heat flux direction at the solidification front. Significant dislocation density is also reported, indicating the relevance of impact dynamics and plastic deformation mechanisms. The comparison with fully-developed coatings suggests a reduction in inter-splat bonding at splat overlapping.

Keywords: Thermal spray, Splat, Crystallisation, Epitaxial growth, Residual stress, Solidification microstructure, Fracture mechanism, Plastic deformation

1. Introduction

Thermal spray methods, e.g. plasma, combustion flame, high-velocity oxyfuel, etc., are widely used to produce thermal, oxidation and wear resistant coatings for many industrial applications, such as aerospace, electronics, energy systems and oil & gas [1, 2, 3, 4, 5, 6]. The material to be deposited is fed, generally in powder form, through a jet stream which melts and accelerates it onto a substrate where it generates a thin layer as it spreads and solidifies. The simplicity and flexibility of the process, in terms of flame temperatures, chemistry and flow, makes it suitable to melt virtually any material and allows the coating properties (e.g. density, chemistry, etc.,) to be tuned over a wide range. Many of the properties of thermally-sprayed coatings depend upon their microstructure (e.g. porosity, oxides, particles' overlapping), which in turn is dictated by the history of mechanical, thermal, and chemical phenomena involved during deposition. Due to the overlapping characteristics of the process and almost independent nature of each impact and solidification event, the problem can be reduced to the analysis of microstructure development at the single splat level (i.e. splat-substrate and successive splat-splat interaction) [7, 8, 9]. In this work, the word "droplet" refers to the in-flight molten particle while "splat" is the same droplet after substrate impact. A single droplet impact event can be described, in thermal spray, as a Rapid Solidification Process (RSP) since it allows continuous quenching while permitting material build-up [10]. The final properties of a solidified splat, namely crystal structure, shape/geometry, residual stress and adhesion are the result of several contributions.

Crystallisation and solidification

Although in RSP, due to the extreme temperature gradient and interfacial velocity of the solidification front, a planar or columnar front growth is often observed (as opposed to dentritic) [11], the specific crystallographic orientation of the splat grains and its relationship with the substrate orientation, if any, is complex to predict. It has been suggested that the establishment of epitaxy in thermally-sprayed materials depends on a combination of substrate crystalline structure, surface temperature and surface melting at droplet impact [12, 13]. A number of studies have addressed the grain structure of thermally-sprayed single splats, mainly focussing on plasma spray and ceramic materials. The effect of substrate preheating on the splat grain structure has also been assessed

*Corresponding author
Email address:* `Dragos.Axinte@nottingham.ac.uk` (D. Axinte)

by Yang et al., [14]. The authors observed that epitaxial Al_2O_3 splats can be formed on $\alpha - Al_2O_3$ substrates at 900°C. Co-Cr coatings have been analysed by Lau et al., [15], where a nanocrystalline structure of 21 nm average grain size was detected by analysis of X-ray diffraction lines. Nanocrystalline structures were also observed in the review of He and Schoenung on $Cr_3C_2 - NiCr$ and Inconel 625 materials [16], who concluded that the origin of these nanostructures still remained an open question. Gang et al., [17] addressed the topic by Transmission Electron Microscopy (TEM) analysis of the texture in FeAl splats from solid and molten powders, observing equiaxed 3D crystallites and elongated 2D nanograins respectively. TEM was also employed in the work of Chraska and King [18, 19] on single and overlapping splats of Yttria Stabilised Zirconia (YSZ) ceramics, occasionally observing epitaxial columnar grains within the subsequent splat by depositing on a preheated stainless steel substrate.

Residual stress

Residual stresses developed in thermal spray can be attributed to two main contributions [20, 21]: quenching stresses, always tensile in nature and generated as the impacting splat contracts during cooling to the substrate temperature, and differential thermal contraction stresses, generated due to differences in thermal expansivity as the splat/substrate system cools-down to ambient temperature. Despite residual stress values having been extensively analysed at a macroscopic level in fully developed coatings, very few studies address the problem at a single splat level. Attempts have been made by Matejicek and Sampath [22] by using X-ray microdiffraction with a 800 μm collimator on plasma- and cold-sprayed Mo and Cu single splats respectively. Residual stresses ranging from 50 to -1050 MPa were measured, increasing in compressive magnitude at higher substrate temperatures. Although X-ray microdiffraction is a well established technique for residual stress measurement, it suffers from being limited to interaction volumes of 50 to 800 μm [23], thus making difficult to reproduce an accurate focus onto small thermally-sprayed splats and assess the stress at an intergranular level (nm in thermally-sprayed splats). Moreover, the residual stress signal acquired in this way is the average from an interaction volume, making it virtually impossible to separate the contributions in different sample directions. More recently, Sebastiani et al., [24, 25], used a novel ring-core drilling method based on Focused Ion Beam (FIB) milling to measure in-plane, depth-resolved residual stresses on ceramic and metallic thermally-sprayed splats. With this technique, residual stresses can be sampled in areas of 3 to 5 μm in diameter, thus considerably smaller than X-ray microdiffraction, although limited to the in-plane direction.

Adhesion

The development of adhesion strength in thermally sprayed single splats can be attributed to three main bonding mechanisms [26, 27, 28]: mechanical interlocking of the splat solidifying within substrate irregularities, chemical bonding due to interdiffusion mechanisms between splat and substrate and physical (or van der Waals) bonding, i.e. weak contributions given by the atomic attraction between splat and substrate. Although mechanical interlocking is often addressed as the major contribution to the overall adhesion strength, the final value of this quantity is also affected by other mechanisms as oxidation, substrate condition and residual stresses. Due to the intrinsic small dimensions of thermally sprayed single splats ($\sim \mu m$), few attempts have been made in research to measure adhesion in these systems, mainly focusing on the application of known techniques generally used for thin films analysis. Balic et al., [29] reported an average strain energy release rate of 80 J/m^2 measured on single splats of Vacuum Plasma Sprayed (VPS) Al_2O_3 material. The value was measured after following the interfacial splat-substrate crack propagation, obtained by indenting the splat via a specifically designed experimental setup. Although a good match was reported in respect to adhesion values experimentally measured by other research groups, the technique is expected to fail in case of strongly adhered splats of ductile materials. A modified ball bond shear test was employed by Chromik et al., [30] to measure fracture strength of Ti splats. Values of up to 240 MPa were measured, largely depending on the droplets' impact velocity. The developed technique is simple as it required little setup, however due to the quite spherical shape of cold sprayed splats (in-flight droplets are largely unmolten at impact with the substrate in cold spray), doubts arise on the application to flat-shaped and/or severely microcracked ceramic splats obtained by other thermal spray techniques. Guetta et al., [31], studied the adhesion of cold sprayed Cu single splats on Al substrates by debonding via a novel LAser Shock Adhesion Test (LASAT) coupled to numerical simulations, obtaining maximum values of 350 MPa. The study demonstrated the development of a quite innovative method for adhesion measurement, although the technique results are difficult to replicate as it requires specific hardware and a calibration step based on finite element analysis.

Thus, although several attempts have been reported in literature to measure crystallisation, residual stress and adhesion in thermally-sprayed single splats, no extensive analysis at a (sub)micrometer spatial resolution for the whole single splat area has yet been carried out. In this paper, a multi-scale approach to the analysis of the crystallisation, residual stress and adhesion is performed, on splat-substrate and splat-splat systems, by using High Angular Resolution Electron Backscatter Diffraction (HR-EBSD) and TEM for crystal orientation, residual stress and geometrically necessary dislocation (GND) analysis and a FIB-milled cantilever beam bending technique for adhesive strength analyses. In this latter

case, fracture strength has been probed at different locations in the splat-substrate interface by using an in-situ indenter inside the SEM chamber. For comparison purposes, residual stress and adhesive strength results are also measured on full coatings, prepared at the same process conditions employed for the single splats, via XRD $sin^2\psi$ and pull-off test respectively. In respect to the previous studies, together with a deep understanding of the phenomena underlying thermal spray processes, this work presents a methodology for the full analysis of all the relevant properties for thermally-sprayed single splats, further providing novel insights into the development of relevant phenomena in thermal spray.

2. Experimental Procedure

2.1. Materials

Commercially available CoNiCrAlY Amperit 415.001 (HC-Starck®) powder, of nominal size 45 ± 22 μm, and Nimonic C263 Ni-based superalloy substrates were used during the experiments because of their widespread use in aerospace industry for thermal barrier coating (TBC) applications (Tab. 1).

Table 1: Chemical composition (wt.%) of powder (Amperit 415.001) and substrate (Nimonic C263) materials used throughout the study.

Commercial Name	Co	Cr	Al	Ti	Y	Mo	Ni
Amperit 415.001	39.0	21.0	8.0	-	0.5	-	bal.
Nimonic C263	20.1	20.6	0.5	2.2	-	5.9	bal.

2.2. Deposition conditions

An oxyacetylene Combustion Flame Spray (CFS) torch (Castodyn® System 2000) was employed as deposition hardware to spray both single splats and full coatings. In the former case, a high torch feed speed was employed in order to obtain a combination of isolated and over-lapped splats. The latter specimens were produced at a lower torch speed (otherwise maintaining the same deposition parameters) with multiple overlapping torch passes, to obtain a final coating thickness of 50 μm. In both cases substrates were vacuum-annealed for 72 h at 1100°C in order to reduce strain gradients for successive residual stress analysis, gently polished with 0.04 μm alumina suspension, degreased with acetone and then preheated to 400°C prior to deposition. This latter preheating stage has been performed in order to obtain disk-shaped splats and further favouring the attainment of epitaxial growth. Single splats were deposited onto $5 \times 5 \times 2$ mm substrates while $\varnothing 25.4 \times 6mm$ cylindrical pieces were employed for full coatings in order to also measure fracture strength via pull-off method. Droplet in-flight velocities and temperatures were measured via a Tecnar® Accuraspray G3C system.

2.3. Characterisation of crystallisation, solidification and residual stress

Both cross-sections and top-views were analysed for the splats. In the former case, samples were prepared from the as-sprayed specimens by a triple ion beam milling system (Leica, EMTIC 3X), set-up at 6 kV and 2.2 mA for 8h, on one edge of the substrate, by previously protecting the splat surface with a glass slide. Splat top-views were prepared by ion-milling at 3° grazing incidence and using 5 kV and 2 mA for 2 h to partially remove the surface oxide layer often present on the as-sprayed splats. HR-EBSD was performed with a dual-beam FIB-FESEM station (Tescan®, Lyra), equipped with an EDAX DigiView IV EBSD camera at 0.10 μm step size, 20 kV beam voltage and 70° specimen tilt with 1×1 or 2×2 binning depending on the size of the analysis area. EBSD post-analysis was performed using the OIM^{TM} 5 software and ad-hoc scripts written in Matlab®. Residual stresses and Geometrically Necessary Dislocation (GND) density were measured by HR-EBSD via cross-correlation-based pattern shift analysis [32, 33, 34] with the BLG® Cross-Court 4 software. GNDs are generated in crystalline materials to maintain local continuity after plastic deformation. Their density (ρ_{gnd}), proportional to the gradient in local lattice rotation (i.e. curvature), can thus be used as a way to quantify the amount of plastic strain stored within the material [35, 36, 37]. In this work, the GND density was calculated from Nye's approach [35], based on lattice curvature tensor determined from cross-correlation pattern shift analysis, and embedded within the software employed for the calculations [37, 38]. It is worth mentioning however, that the density so obtained represents a lower bound of the total dislocation density [39]. In-plane macroscopic residual stress was measured on full coatings via the $sin^2\psi$ method on a Bruker® D8 advance machine. In this case, assuming plane stress conditions, a diffraction angle $2\theta = 93.16°$ was maintained, corresponding to the (311) reflection, with Young's modulus and Poisson ratio set at 215 GPa [25] and 0.3 respectively. TEM samples of single splat cross-sections were prepared by FIB liftout (Tescan, Vela). Scanning-TEM (STEM) and Energy Dispersive X-ray (EDX) mapping were carried out in a JEM2200fs microscope (JEOL).

2.4. Characterisation of adhesion

Microcantilever beams were prepared using the FIB on the splat cross-sections with ion currents ranging from 800 pA down to 10 pA (rough to fine milling) at an acceleration voltage of 30 kV. Three splats were tested, for a total of 23 microcantilevers, spaced approximately 15 μm apart and milled at several places in the splat-substrate interface. An approximate l:w:t ratio of 4:1:1.5 was targeted for all cantilevers (Fig. 10), while real dimensions were measured from SEM micrographs. Prior to the tests the crystal orientation was evaluated via EBSD analysis. The cantilevers were loaded using an Alemnis nanoindenter (Alemnis GmbH), equipped with a cube-corner tip
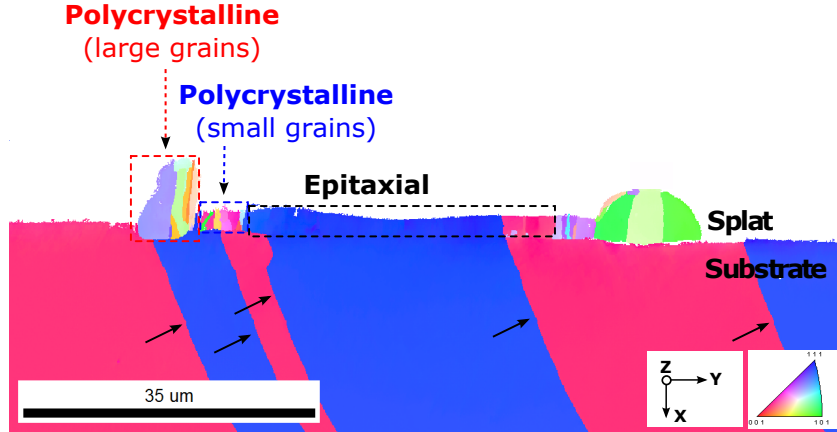
Figure 1: EBSD IPF (X) map of a single-splat cross-section, showing several crystallisation regions and $\Sigma 3$ twin boundaries within the substrate (black arrows).

driven at 0.05 $\mu m/s$ displacement rate. Macroscopic fracture strength was measured on full coatings via a pull-off method following the ASTM C633 standard on 6 specimens.

3. Results and Discussion

3.1. Crystallisation

3.1.1. Single splat cross-section

The EBSD Inverse Pole Figure (IPF) map in the vertical direction (X) of a typical splat cross-section is shown in Fig. 1. The map shows the presence of $\Sigma 3$ twin boundaries within the substrate (black arrows), as expected from low stacking fault energy of Ni-superalloys [40, 41]. Interestingly, a wide internal region of epitaxial growth, covering $\sim 75\%$ of the splat-substrate interface, is observed (the splat/substrate epitaxial relationship in this area has further been confirmed by the IPF-Y and -Z maps), facilitated by the similar lattice parameter between splat and substrate materials, reported showing a γ face-centred-cubic (fcc) matrix structure of 0.356 and 0.358 nm [42, 43]. At the edges of this epitaxial zone, areas of polycrystalline growth are found, with grain size increasing towards the splat rim. Each of these regions have been determined, to cover approximately $\sim 12.5\%$ of the whole interface area. The establishment of epitaxy is also revealed by the Bright-field STEM (BF-STEM) micrograph in Fig. 7. In the same figure, alumina oxide, probably generated in-flight on the splat surface or grown post-deposition [44], is present as a white band on top of the splat, as confirmed by EDX analysis. Epitaxial growth is a special crystallisation process where grains are required to grow quick enough so that the establishment of nucleation sites is hindered. Predicting the growth rate of an epitaxial and/or nucleated solidification front is non-trivial, due to the interplay of several factors: material thermo-mechanical properties, crystal orientation, undercooling degree, substrate temperature and contact angle, which vary continuously and locally, at the front of solidification. Clearly, for the

splat under analysis, a rapid growth of the epitaxial front has been achieved in the central region (i.e. the first impact point), overcome by growing nucleated clusters in the external regions. The observation of epitaxial growth suggests that an intimate splat/substrate contact has been achieved during solidification. Interdiffusion is thus likely to have happened, enhanced by the high temperatures experienced during the process. This is confirmed by the EDX scan over a TEM image taken at the splat/substrate interface within the epitaxial region, Fig. 2. In the figure, the splat/substrate interface is located by a darker line corresponding to a higher density of dislocations. The inset depicts EDX profiles for Mo and Ti corresponding to the black dashed line profile in the image. A region of compositional gradient, spanning ~ 200 nm is clearly observed, confirming the presence of interdiffusion. Due both to a decreasing impact pressure from the centre and reduced temperature of the flattening splat with time, less interdiffusion is expected towards the rim region. Here the establishment of metallurgical bonding can additionally be hindered by the presence of oxide present as a shell on the droplet surface and displaced, at impact, towards the edges [44].

3.1.2. Top-view and overlapped splats

The grain texture is determined by the direction of heat flux at the solidification front and can be thus examined to evaluate the thermal exchange history during splat formation [11]. A qualitative understanding is given by the EBSD (X) map of a solidified splat in top-view (Fig. 3). In the figure, the approximate edges of the three solidification zones in Fig. 1 are also depicted (bottom left side). Clearly, a symmetric solidification trend is not observed for the whole splat as a polycrystalline area is observed on the left side while epitaxial growth dominates the right region. Non-indexed areas in the map correspond both to oxidised material (within the splat) and localised regions of large deviation from the 70° tilt angle (at the splat perimeter). Interestingly, the epitaxial zone shows areas of marked
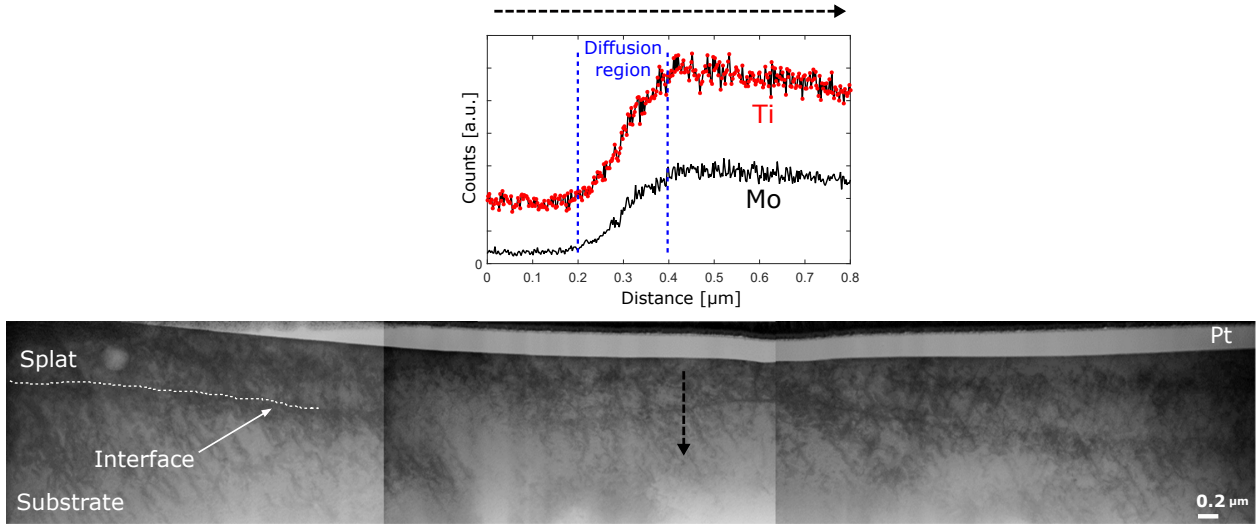
Figure 2: Bright Field (BF)-STEM image of splat/substrate cross-section interface within the epitaxial crystallisation region; the EDX profiles for Mo and Ti (inset) demonstrate a diffusion region of $\sim 200\ nm$ between the two systems, suggesting a strong metallurgical bonding.

misorientation, which correspond to low-angle boundaries. Local misorientation measurements confirm the presence of steep orientation changes of maximum $\sim 6.5°$ throughout the area. The result would suggest that this region is composed of separately growing epitaxial grains coalescing at percolation, which is similar to what observed in supersaturated thin films deposited from vapour phase precursors, i.e. a Volmer-Weber growth type [45]. The presence of epitaxial domains of different orientations is generally linked to defects on the substrate surface prior to deposition or to compositional variations at the solidification front caused by interdiffusion with the substrate [46, 45]. In this study, the mirror-polished substrate surface was preheated prior to deposition, a factor that would reduce the effect of surface defects, thus suggesting a prevalent influence of interdiffusion.

Grains in the polycrystalline small-grained zone are prevalently isolated and of random orientation, suggesting heterogeneous nucleation over a surface oxide layer (as previously determined by EDX analysis) and growth in a direction perpendicular to the substrate surface. However, there seems to be a growth relationship between these grains, as made clear by the prevalence of $\Sigma 3$ boundaries in this zone (as assessed from a separate analysis on the IPF map). The same orientation relationship is not maintained between grains in the polycrystalline large-grained zone, where instead high-angle boundaries are predominantly observed. Moreover, the grains in this latter zone are elongated in shape, varying from a smaller dimension close to the area of small grains and becoming enlarged
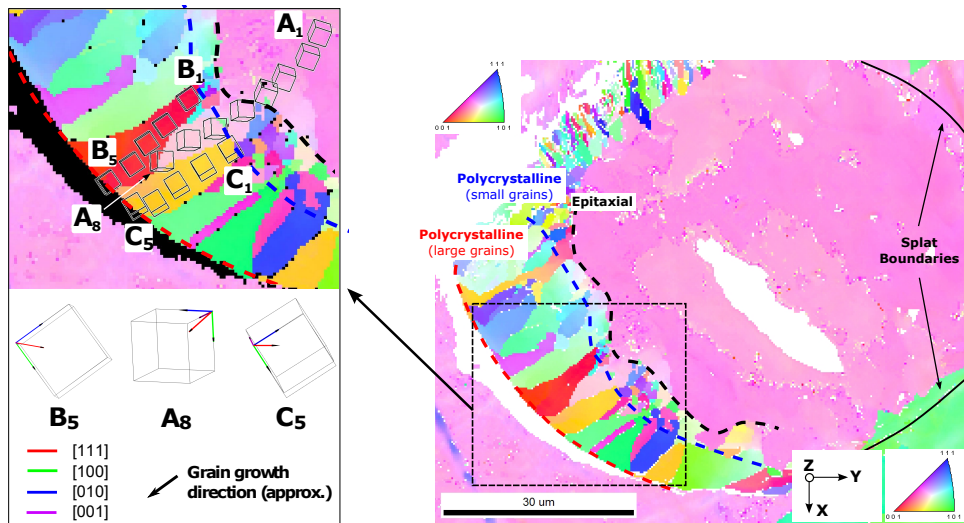
Figure 3: EBSD IPF (X) map with overlapped grain boundaries character of a typical splat top-view showing the three crystallisation regions. The extensive presence of low-angle boundaries within the epitaxial region is shown, moreover, the choice of $<100>$ as preferential crystallographic growth direction is demonstrated in the inset.

5

towards the far edge of the splat. This demonstrates that, in this zone, the solidification front moves radially in a direction close-to-parallel with respect to the deposition surface. A schematic diagram showing the heat flux direction and solidification front is depicted in Fig. 4 at different stages of the process. A poor contact with the substrate, as
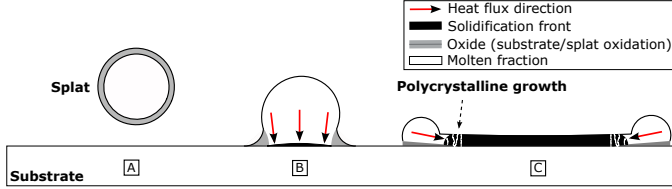
Figure 4: Schematic view of effects from heat flux and surface oxide layer on solidification characteristics at different time steps during droplet impact and flattening.

previously determined, would favour the establishment of heat fluxes radially through the solidified material towards the centre of the splat as opposed to perpendicular transfer expected in the epitaxial and small-grained areas. Moreover, a poor contact experienced by the solidifying material in the large-grained zone would suggest a corresponding low crystallisation undercooling of the molten fraction [47]. Since a small undercooling is linked to low nucleation rate, the absence of crystallites in this external zone is explained. Similarly, the presence of smaller crystallites in the polycrystalline (small grained) area would suggest a higher melt undercooling, provided by the vicinity to the well-adhered epitaxial zone. In order to better describe the attainment of the observed texture, changes in the local crystallographic orientation can be locally mapped. In the inset of Fig. 3, the local orientations of the unit cell are depicted at several locations within three grains: (A) nucleating into the epitaxial zone and stopping within the area of large grains, and (B) and (C) nucleating in the polycrystalline (small grained) area and extending to the splat rim. The high misorientation observed between the cells A_1 and A_8 supports the assumption that a change in heat flux direction is experienced during solidification from the epitaxial region to the peripheral regions. This is further confirmed by grains B and C, whose solidification starts within the polycrystalline region of small grains and for which a change in misorientation is, in fact, not observed. It is also worth noting that the growth of grain A ends in the middle of the polycrystalline zone of large grains, while grains B and C grow until the splat rim. The reasons for this behaviour can be related to the preferential character of solidification direction, as depicted in the inset of the figure. The principal axis orientations for the three external cells A_8, B_5 and C_5: while cells B_5 and C_5 present a solidification growth aligned with the $[0\bar{1}0]$ direction, A_8 shows [111] instead. Since the $[0\bar{1}0]$ direction is also observed in all the other crystallites within the zone of large grains (not depicted), it can be concluded that this represents the fastest solidification direction under the experimental conditions of this study. Theoretically, from a

surface energy standpoint in ideal vacuum, {111} planes are more stable than {100} families in fcc crystals of Ni [48]. However, it is demonstrated in this work that surface energy minimization cannot be addressed as unique driving factor for preferential solidification orientation in RSP, where kinetic factors are likely to play a significant role. A preferential growth in the < 100 > direction is generally reported in literature for thermally-sprayed Ni-Cr materials [49], thus confirming the findings of this work.

The solidification behaviour has been further qualitatively analysed in the case of two subsequently impacting splats, as depicted by the IPF (X) map in Fig. 5. Interest-
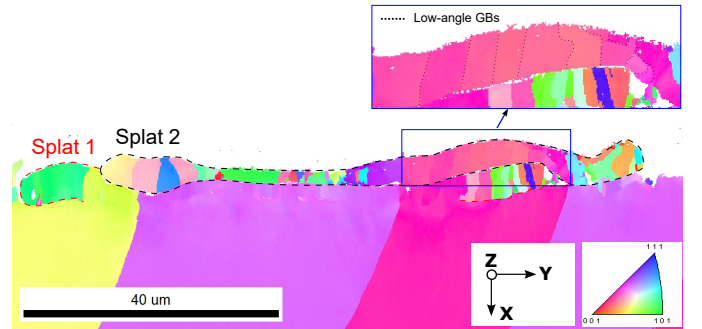
Figure 5: EBSD IPF (X) map of a cross-section obtained on two overlapped splats, showing partial attainment of epitaxy and presence of low-angle boundaries within the second splat.

ingly, an epitaxial region is still observed within the second incoming splat. However, this area is not formed homogeneously in the central impact zone, but extends on top of a polycrystalline area at the edge of the first splat. Moreover, the significant presence of low-angle grain boundaries is again observed (see inset), further confirming the findings of the single splat (Fig. 3). The inhomogeneity in crystal growth observed in the second splat is likely connected to instabilities both in the flattening dynamics (due to the rough profile of the first splat) and presence of oxide on the impact surface (generated in-flight or after impact of the first splat) [44].

3.2. Plastic strain and residual stress

3.2.1. Single splat cross-section

The calculated GND density is reported in the map of Fig. 6(a). Note that in the figure, the analysis has excluded grains within the splat polycrystalline areas, due to the impossibility, for these grains, to select an unstrained reference pattern within the substrate from a grain of the same crystallographic orientation. The highest GND density is located within the splat itself and in the first tens of microns underneath it as opposed to the substrate surfaces outside of the splat area. A high density is found in the middle portion of the splat, with values as high as $2 \cdot 10^{15}$ m^{-2} as determined by HR-EBSD. A decreasing value is observed vertically, with values decreasing to $7 \cdot 10^{14}$ m^{-2} deep within the substrate. The high density measured within the first tens of μm underneath the splat
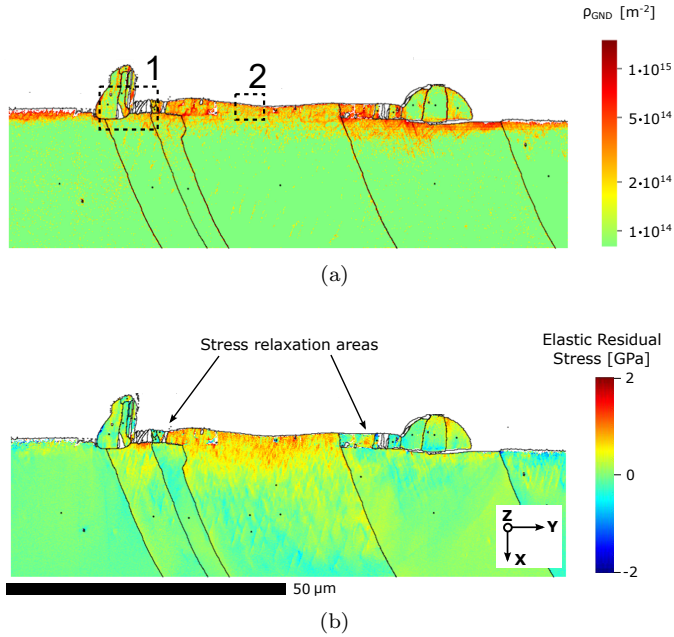
Figure 6: **(a)** Distribution of GND density within and below the single splat cross-section in Fig. 1 showing the tendency for slip system activation; marked regions correspond to the areas of TEM imaging in Fig. 7. **(b)** In-plane σ_Y linear elastic residual stress for the same system, exhibiting a radially decreasing trend from the splat centre and low magnitude at locations corresponding to the onset of polycrystalline growth (stress relaxation areas).

confirms the high plastic strain experienced in this area, with averages values around $9 \cdot 10^{14} \ m^{-2}$. Interestingly, the highest density in this area is found underneath the right edge of the splat as opposed to the central region, probably due to a local unbalance in impact pressure. The dislocation density seems generally spatially confined in lines of specific direction (see the substrate grain immediately below region 1 in the figure), possibly indicating the activation of plastic slip.

Higher spatial resolution of GND density is achieved by TEM analysis of the regions labelled 1 (polycrystalline) and 2 (epitaxial) in Fig. 6(a), as reported in Fig. 7. The unit cell corresponding to the crystal orientation of both regions is depicted in the inset, together with the traces of the four slip planes available for fcc crystals. Region 1 shows the dominance of both $(1\,1\,\bar{1})$ (light blue) and $(\bar{1}\,1\,1)$ (green) slip traces over $(\bar{1}\,\bar{1}\,1)$ (red) and $(1\,1\,1)$ (purple). However, this latter is observed within the first micron from the interface, suggesting a complex direction of load application caused by splat impact. A combination of dislocations lying on the $(1\,\bar{1}\,1)$ slip system, as well as dense dislocation groups are instead observed in region 2. Due to the epitaxial growth from a molten phase in this region, dislocation activity is likely connected to stress relaxation effects, rather than the impact-induced plastic deformation. Misfit and threading dislocations, non-equilibrium defects commonly observed in heteroepitaxial thin film structures, are also considered contributing to the over-

all dislocation generation and multiplication mechanism, giving rise to the observed complex interaction [50, 51]. A high density of pinned dislocations is also observed pinning at the splat-substrate interface. It is hypothesized here that coherency stresses present in this area present a potential barrier for moving dislocations, generating a mismatch in slip planes between splat and substrate lattices [52]. The linear elastic residual stress state normal component in the specimen Y (in-plane) direction is depicted in Fig. 6(b). Although a marked tensile stress level is observed in the whole region, concentrated within and in the area below the splat, some other relevant features can be noticed. Vertically from the top splat surface, a decreasing residual stress level is found from $\sim 2 \ GPa$ and almost vanishing deep within the substrate (as expected since this latter region was selected as the approximate location for the cross-correlation analysis reference point). The stresses within the splat, particularly within the central area, are high $\sim 1.5 \ GPa$ if compared to the yield stress generally reported for Ni-superalloy materials ($\sigma_y \sim 0.8 - 1.2 \ GPa$ [53]), suggesting that plastic strain has occurred. Particular attention has to be taken when measuring residual stress by HR-EBSD in plastically deformed materials due to large misorientation [54]. However, the maximum misorientation in the splat compared to the reference pattern is below $3°$ within the central grain, making the application of remapping not required [54]. It is worth noting that the stress level within the splat markedly decreases to almost zero at the edges of the epitaxial zone. A reduction in stress is expected in these zones, possibly due to the combined effect of stress relieving phenomena (edge curling) and low splat-substrate adhesion caused by the transition to heterogeneous nucleation over an oxidised surface [21]. Finally, the substrate residual stress level in an area immediately below the splat shows general tensile character, with gradually decreasing intensity from the splat centre. The highest stresses measured in this area, although of lower magnitude compared to within the splat, are also found to exceed the material yield stress at several points, confirming the potential attainment of plastic strain. The overall system elastic stress behaviour is summarised in Fig. 8(a). Literature data on the topic is scarce both due to the current lack in analytical techniques able to probe residual stress at the single splat level and the wide range of materials and deposition conditions tested. The only meaningful comparison was found in the work of Sebastiani et el., [25], who reported an in-plane tensile residual stress on the order of $100 \ MPa$ (i.e. difference of one order of magnitude in respect to this work) in plasma-deposited single splats of Ni-5%Al onto polished and preheated stainless steel substrates, measured through an innovative FIB-milling method. As a possible explanation, the compared systems, in terms of materials (Ni-Al/Stainless steel vs CoNiCrAlY/Ni-superalloy of this work) and deposition conditions (plasma- vs flame-spray of this work) are inherently different. Epitaxy for instance, observed in this work
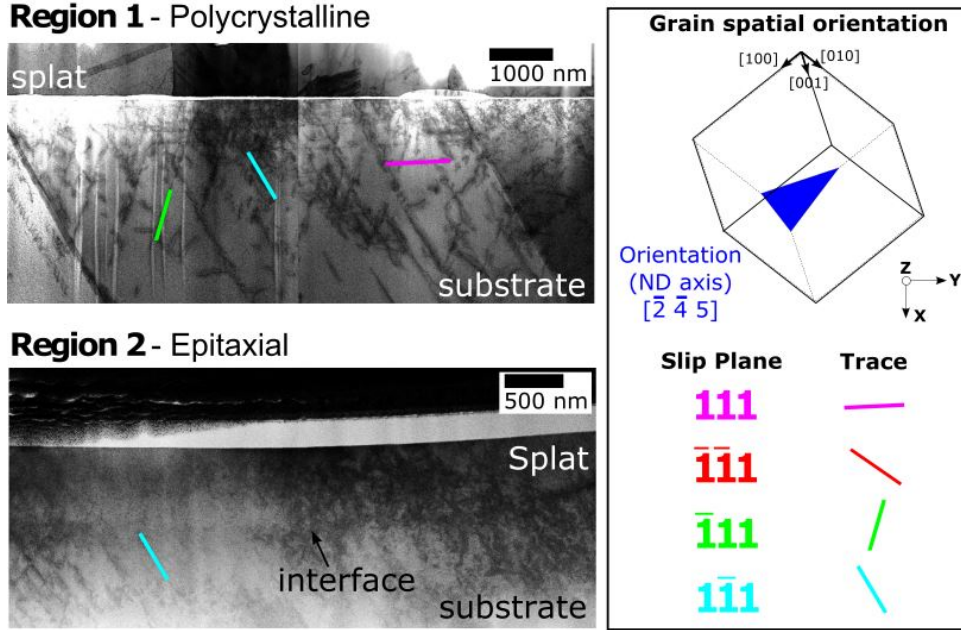
Figure 7: BF-STEM image of the two regions highlighted in 6(a). The prevalence of primary and secondary slip system activation is observed in the polycrystalline region (1) while a combination of primary slip combined with dense bundles is predominant within the epitaxial region (2). Relevant crystallographic planes and directions are depicted in the unit cell.

and not reported by [25], could be a major factor influencing the development of residual stress [45]. Secondly, the reference pattern chosen for cross-correlation strain analysis (far inside the substrate) might not be strain-free as assumed, so that the high stresses measured in Fig. 6(b) could be not correctly quantified. Although in this work the reference pattern was selected, for each grain, within an area of low misorientation far inside the substrate as determined from High-Resolution Kernel Average Misorientation (HR-KAM) mapping, the choice might not be sufficient to ensure quantitative accuracy.

Attempting to predict residual stress from theoretical principles is not a trivial task. Together with difficulties connected to the above mentioned reference pattern selection, the complexity of the crystal growth phenomenon, where behaviour depends on material system and solidification parameters, has to be addressed. Extrinsic stresses, linked to the thermal difference between splat and substrate, are assumed here to be mainly the result of quenching, thus accounting for the rapid contraction while reaching substrate temperature. In fact, the influence of thermal contraction (i.e. the contribution to residual stress due to the splat/substrate system cools-down to ambient temperature) is neglected in this study due to the expected similarity in thermal expansivity for the splat and substrate materials [45]. Intrinsic stresses are generated due to thermodynamic instabilities developed during crystal growth both within the epitaxial and polycrystalline splat areas [21]. Sources for this type of stress are mainly related to splat-substrate lattice parameter mismatch (within the first nm of film thickness, [45]), domain wall formation between growing crystals (in the epitaxial zone) and small

misorientation at the grain boundary between adjacent grains (polycrystalline zones) [55]. Finally, stress relaxation mechanisms, namely edge relaxation and yielding are here considered playing a fundamental role in reducing the stress within the splat. The quenching stress can be calculated as [21]:

$$\sigma_q = \alpha_p \Delta T E_p = 6.8 \, GPa \qquad (1)$$

with splat thermal expansivity $\alpha_p = 15 \cdot 10^{-6} \, °C$ [56], splat-substrate (measured) temperature difference $\Delta T = T_p - T_{sub} = 2500 - 400 = 2100 \, °C$ and Young's modulus $E_p = 215 \, GPa$ [25]. Thus, a significant tensile stress is calculated within the splat, considerably above the maximum values previously measured ($\sim 2 \, GPa$). It is likely that this overestimation is linked to the influence of additional residual stress mechanisms. Since in Eq. 1, residual stress contributions due to domain walls (intrinsic, generally compressive in nature [45]), edge curling, yielding and creep (relaxation mechanisms) have not been included, it is likely that their contribution cannot be safely neglected if an accurate prediction is needed. Moreover, while edge curling was confirmed by direct observation of SEM micrographs, the occurrence of yielding is demonstrated by both the high GND density and residual stress probed within the splat. The significant contribution of stress relaxation mechanisms toward lowering the measured value of residual stress from theoretical predictions is commonly reported in thermal spray literature of metallic coatings [21]. Due to the high tensile stress measured, quenching is here assumed to represents the main source of induced residual stress. Moreover, intrinsic stresses are generally active only within the first $\sim 100 \, nm$ of film growth, and thus

8

(a)

(b)
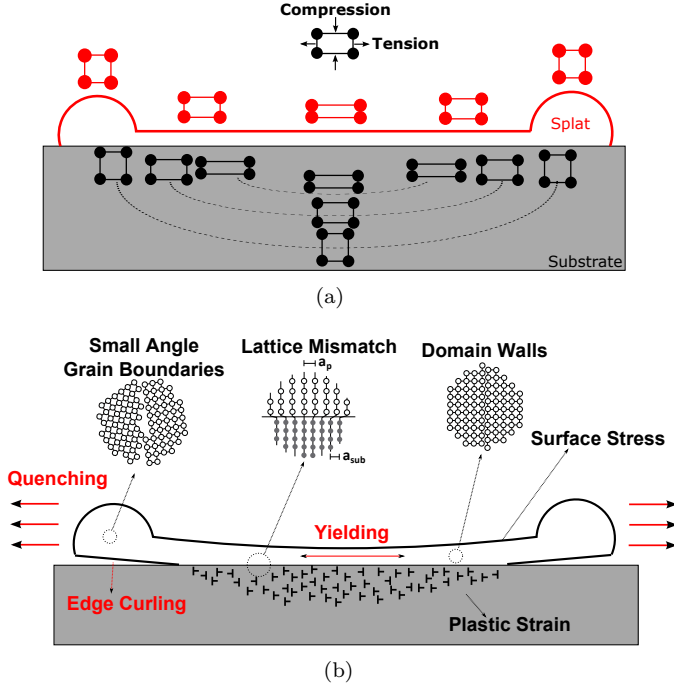
Figure 8: **(a)** Schematic representation of the tensile in-plane elastic residual stress within splat and substrate after solidification and **(b)** fundamental mechanisms responsible for residual stress build-up during deposition; primary contributions are attributed to quenching, yielding and edge curling.

(a)

(b)

Figure 9: **(a)** Distribution of GND density within and below the overlapped splat cross-section in Fig. 5, showing an increased plastic activity with respect to the single splat (Fig. 6(a)). **(b)** In-plane σ_Y Linear elastic residual stress for the same system, showing areas of mixed stress character (inset) and general lower magnitude within the second splat due to the weak bonding to the first splat.

do not to appreciably affect the thicker films ($\sim 1000\ nm$) of this work [45].

3.2.2. Overlapped splats

The in-plane σ_Y residual stress component for overlapped splats is depicted in Fig. 9(b). The stress within the first splat shows alternating compressive and tensile regions. As depicted in the inset, the latter are localised above unmapped areas within the splat, probably representing cavities generated by gas entrapment from the impact of the second splat. A similar alternating trend is observed within the substrate, where lower magnitudes in respect to the single splat case are measured (~ 0.7 vs $\sim 2\ GPa$ respectively). Moreover, as shown in Fig. 9(a), dislocation densities are found to spread deeper within the substrate with respect to the single splat case (Fig. 6(a)). Larger plastic deformation compared to the single splat may induce more uncertainty for an unstrained reference frame, thus making the measured absolute value of residual stress inaccurate. Finally, it is worth noting that a very low stress is detected within the second splat, suggesting a tendency to residual stress reduction at splat overlap. The effect can be attributed to lower inter-splat adhesion compared to splat-substrate, caused by the presence of oxide and other deposition impurities over the surface of the first splat [44].

3.2.3. Comparison to coatings

The $sin^2\psi$ technique was used to measure residual stresses in fully developed coatings sprayed at the same conditions previously employed for the single splats. A considerably lower stress (0.18 GPa) is measured within the coating, as compared to the single splat (0.5-1.5 GPa, Fig. 6(a)), possibly due to lower intersplat adhesion [44]. Moreover, since in-plane stresses are probed by XRD analysis, the determined stress is the result of several contributions, including splat, pores, etc. The coating residual stress data are comparable to literature data on similar systems, sprayed on substrates grit-blasted prior to deposition, as opposed to the polished ones of this study [21]. This would suggest that the strong influence of epitaxy on residual stress at the single splat level is reduced by coating build up.

3.3. Adhesion

3.3.1. Single splat

In order to get a better estimate for the local adhesion distribution within the single splat, microcantilever beam-bending tests have been performed. A SEM micrograph of a cantilever milled in within the polycrystalline zone of a single splat is shown in Fig. 10. As depicted in the inset, the polycrystalline nature of solidification can be appreciated by EBSD mapping. Following the linear-elastic bending theory of clamped beam of Matoy et al., [57], the maximum bending stress σ at the splat-substrate interface

9

can be obtained as:

$$\sigma = 6\frac{F\,l}{w\,t^2} \tag{2}$$

where F is the applied load, l the bending length, w and t the cantilever beam width and thickness respectively (Fig. 10). Based on the solidification zone where the cantilever
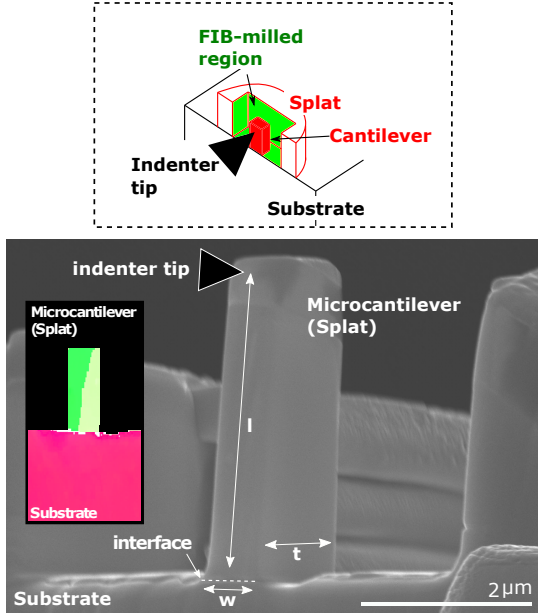
Figure 10: SEM micrograph showing geometric dimensions and loading conditions for cantilevers with a ratio $l/w \sim 6$. The crystallographic orientation of each cantilever has been determined by EBSD (inset).

was milled, three different load-displacement behaviours were determined (Fig. 11). Within the epitaxial area (black curve), after an initial linear elastic region, plastic deformation sets in, confirmed by the presence of slip lines at the cantilever base. No interface crack propagation was observed in any of the tested specimens, as further demonstrated by the absence of load drops in the curves. Due to the absence of a critical load F_c for the application of Eq. 2, in this case an ad-hoc value was determined at 95% of the curve slope in the linear elastic region; the adhesion strength obtained in this way would thus represent an underestimation of the exact value. On the other hand, a load drop is observed within the polycrystalline zone outside the epitaxial area (blue curve), representing the interfacial crack initiation. In this case, the critical load F_c was defined as the load drop value. Finally, no load is recorded for cantilevers belonging to the polycrystalline zone at the splat rim (red curve), suggesting that very low adhesion was present before indentation.

The calculated fracture strength versus normalised splat radius is reported in Fig. 12 for all the 23 cantilevers and solidification zones tested. Linear fits within each zone are also reported, together with the norm of the residuals. Interestingly, the strength is found to increase from the splat centre to the edge of the area within the epitaxial zone,
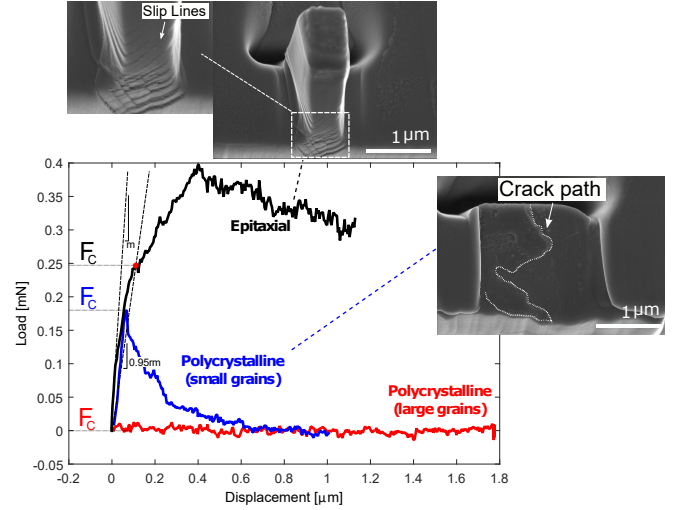
Figure 11: Typical load-displacement curves obtained from cantilevers milled in the three crystallisation regions of a single splat, with respective post-bending SEM micrographs at the interface location. No crack propagation is observed within the epitaxial area, thus the critical load F_C is selected at 95 % of the slope in the elastic region. A mixed-mode fracture and no crack propagation are instead characteristic of the polycrystalline-small-grains and -large-grains regions respectively.

probably linked to impact pressure and temperature effects. On the other side, the expected decreasing fracture strength is found within the polycrystalline area of small grain size (blue). In this case, a lower adhesion value with respect to the epitaxial zone and decreasing towards the external rim, is expected due to lower splat-substrate interdiffusion and edge curling stress relaxation.

3.3.2. Comparison to coatings

The pull-off adhesion testing method was employed to measure fracture strength in $\sim 300\ \mu m$ coatings sprayed at the same conditions employed for the single splats in this study. For comparison, an averaged single splat value of 2.2 GPa has been obtained from the results of Fig. 12, with values of 2.5 GPa (epitaxial zone, covering 75 area%), 2 GPa (polycrystalline small-grains zone, covering 12.5 area %) and 0 GPa (polycrystalline large-grains zone, covering 12.5 area %). Results show values of 0.16 and 2.2 GPa for coating and single splat respectively. A metallographic inspection of the pull-off specimens fractured surface reveals that either fully cohesive or mixed-mode delamination is predominantly experienced. Several factors can contribute to the observed difference. The tensile loading conditions experienced by the application of the two testing methods would suggest little discrepancies in measured strength. However, lower adhesion is expected from testing a coating in respect to a single splat due to the substantially higher density of defects (e.g. pores, microcracks, etc.), which act as sources of crack initiation. Moreover, the strong adhesion provided by epitaxial solidification, together with the lower adhesion expected at coating build-up would explain the cohesive nature of crack propagation. From a residual
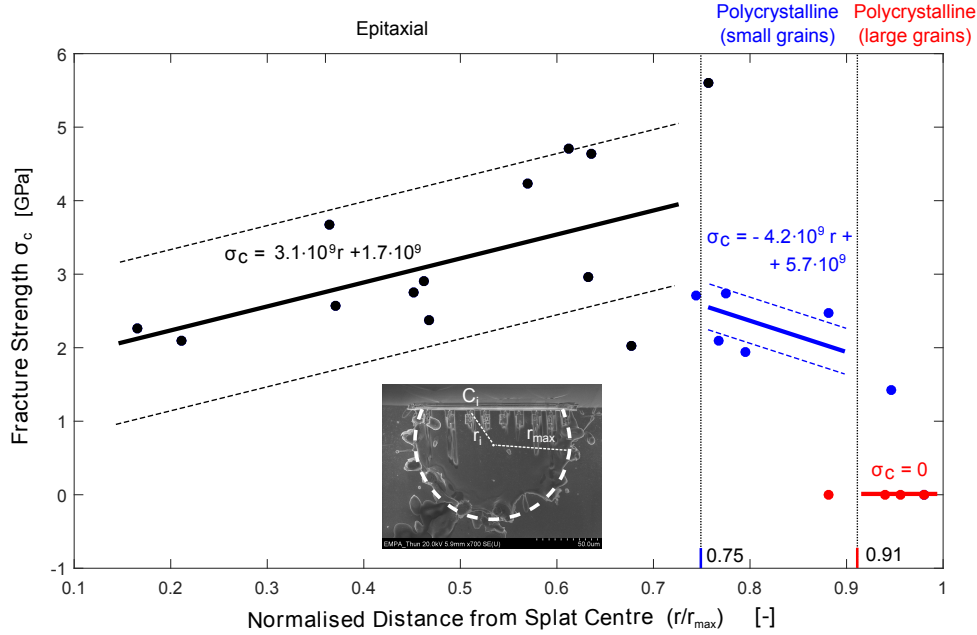
Figure 12: The calculated fracture strength shows a general decreasing magnitude with splat radius. Geometrical parameters, including splat radius r_{MAX}, and cantilever index C_i and radius r_i are depicted in the inset. The uncertainty was determined as standard error of regression in each region.

stress perspective, tensile in-plane residual stresses, which are measured in these coatings but are likely to be absent in cantilevers milled from single splats, could also contribute to lowering the measured fracture strength.

4. Conclusions

An in-depth study to understand and quantify crystallisation, residual stress and adhesion in epitaxial CoNiCrAlY flame-sprayed systems, both for single and overlapped splats, has been performed. HR-EBSD and TEM analysis have been employed for the analysis of crystallisation and solidification texture. The same techniques, allowing one to resolve features at sub-micron scale, are further employed to measure residual stress and connected dislocation development characteristics. A microcantilever beam bending technique is employed to quantify fracture strength at several locations within the splat/substrate interface. The findings were linked to measurements performed on fully developed coatings, sprayed at the same process conditions employed for single splats, via $sin^2\psi$ and pull-off tests for residual stress and fracture strength respectively. In particular, the research has highlighted the following key findings:

- Different crystallisation regions are observed in the single splat: epitaxial, polycrystalline-small and -large grains covering 75, 12.5 and 12.5 % of the interface respectively. This partition is attributed to both the effect that impact pressure and temperature have on interdiffusion at the splat/substrate interface and the influence of oxide generated in-flight on the droplet surface,

- Plastic deformation is observed both within the splat and the substrate, with dislocation densities on the order $\rho \sim 10^{14} - 10^{15}\ m^{-2}$. Within the splat, plasticity is mainly attributed to yielding during solidification, while impact pressure and temperature are held responsible for the substrate. In the latter, primary and secondary slip are observed as the main sources of dislocation activity. An increase in dislocation density is observed in the case of overlapped splats, as expected at an increase in impact pressure,

- A tensile in-plane linear elastic residual stress, reaching maximum levels of $\sim 1-2\ GPa$ is measured both within the splat and in the substrate, in this latter case decreasing radially from the splat centre. The lower magnitude compared to theoretical quenching stress ($6.8\ GPa$) confirms the marked influence of stress relaxation mechanisms. A moderate residual stress is measured for the overlapped splat, and this is linked to less interaction (i.e. adhesion, chemical interdiffusion) with the previously deposited splat,

- A gradient in fracture strength has been measured from average values of $\sigma_c \sim 2.5\ GPa$ in the epitaxial region, rapidly decreasing to $\sigma_c = 0\ GPa$ in the polycrystalline-large-grains zone. The values are justified by the cantilevers behaviour at loading: plastic bending (epitaxial region), mixed-mode interface crack propagation (polycrystalline-small-grains) and absence of crack propagation (polycrystalline-large-grains),

- A considerably lower residual stress, 0.18 GPa, is measured in a full coating compared to a single splat,

11

which is attributed to an enhanced activation of stress relaxation mechanisms (e.g. interfacial sliding and edge relaxation), made possible by the lower degree of chemical-mechanical interaction observed at subsequent splat overlaps. The lower interaction between overlapped splat, together with the higher density of defects, are held responsible for a lower coating fracture strength, 0.16 GPa, as compared to a single splat.

5. Acknowledgments

References

[1] F. Fanicchia, D. A. Axinte, J. Kell, R. MvIntyre, G. Brewster, A. D. Norton, Combustion flame spray of conicraly & ysz coatings, Surface and Coatings Technology 315 (2017) 546–557.

[2] N. P. Padture, M. Gell, E. H. Jordan, Thermal barrier coatings for gas-turbine engine applications, Science 296 (2002) 280–284.

[3] S. Sampath, Thermal spray applications in electronics and sensors: Past, present, and future, Journal of Thermal Spray Technology 19(5) (2010) 921–949.

[4] P. Ernst, G. Barbezat, Thermal spray applications in powertrain contribute to the saving of energy and material resources, Surface and Coatings Technology 202 (2008) 4428–4431.

[5] R. Vaßen, H. Kaßner, A. Stuke, F. Hauler, D. Hathiramani, D. Stöver, Advanced thermal spray technologies for applications in energy systems, Surface and Coatings Technology 202 (2008) 4432–4437.

[6] H. Herman, S. Sampath, R. McCune, Thermal spray: Current status and future trends, MRS Bulletin.

[7] R. C. Dykhuizen, Review of impact and solidification of molten thermal spray droplets, Journal of Thermal Spray Technology 3(4) (1994) 351–361.

[8] V. V. Sobolev, J. M. Guilemany, Flattening of droplets and formation of splats in thermal spraying: A review of recent work − part 1, Journal of Thermal Spray Technology 8(1) (1999) 87–101.

[9] V. V. Sobolev, J. M. Guilemany, Flattening of droplets and formation of splats in thermal spraying: A review of recent work − part 2, Journal of Thermal Spray Technology 8(1) (1999) 301–314.

[10] M. Moss, Dispersion hardening in Al-V by plasma-jet spray-quenching, Acta Metall. Mater. 16 (1968) 321–326.

[11] M. Cohen, R. Mehrabian, Some fundamental aspects of rapid solidification, Rapid Solidification Processing: Principles and Technologies III (1980) 1–26.

[12] W. Zhang, G. Wei, H. Zhang, L. Zheng, D. Welch, S. Sampath, Toward the achievement of substrate melting and controlled solidification in thermal spraying, Plasma Chemistry and Plasma Processing 27 (2007) 717–736.

[13] E. Yang, X. Luo, G. Yang, C. Li, M. Takahashi, S. Kuroda, K. Kim, Impact of deposition temperature on crystalline structure of plasma-sprayed Al_2O_3 splats revealed by FIB-HRTEM technique, Ceramics International 42 (2016) 853–860.

[14] E. Yang, X. Luo, G. Yang, C. Li, C. Li, M. Takahashi, Epitaxial grain growth during 8YSZ splat formation on polycrystalline YSZ substrates by plasma spraying, Surface and Coatings Technology 274 (2015) 37–43.

[15] M. L. Lau, E. Strock, A. Fabel, C. J. Lavernia, E. J. Lavernia, Synthesis and characterization of nanocrystalline co43 coatings by plasma spraying, Nanostructured Materials 10(5) (1998) 723–730.

[16] J. He, J. M. Schoenung, Nanustructured coatings, Materials Science and Engineering A 336 (2002) 274–319.

[17] J. Gang, J. P. Morniroli, T. Grosdidier, Nanostructures in thermal spray coatings, Scripta Materialia 48 (2003) 1599–1604.

[18] T. Chraska, A. H. King, Transmission electron microscopy study of rapid solidification of plasma sprayed zirconia − part I. first splat solidification, Thin Solid Films 397 (2001) 30–39.

[19] T. Chraska, A. H. King, Transmission electron microscopy study of rapid solidification of plasma sprayed zirconia − part II. interfaces and subsequent splat solidification, Thin Solid Films 397 (2001) 40–48.

[20] T. W. Clyne, S. C. Gill, Residual stresses in thermal spray coatings and their effect on interfacial adhesion: A review of recent work, Journal of Thermal Spray Technology 5 (1996) 401–418.

[21] S. Kuroda, T. W. Clyne, The quenching stress in thermally sprayed coatings, Thin Solid Films 200 (1991) 49–66.

[22] J. Matejicek, S. Sampath, Intrinsic residual stresses in single splats produced by thermal spray processes, Acta Materialia 49 (2001) 1993–1999.

[23] D. Lau, D. Hay, N. Wright, Micro x-ray diffraction for painting and pigment analysis, AICCM Bulletin 30.

[24] M. Sebastiani, C. Eberl, E. Bemporad, G. Pharr, Depth-resolved residual stress analysis of thin coatings by a new FIBDIC method, Materials Science and Engineering A 528 (2011) 7901–7908.

[25] M. Sebastiani, G. Bolelli, L. Lusvarghi, P. Bandyopadhyay, E. Bemporad, High resolution residual stress measurement on amorphous and crystalline plasma-sprayed single-splats, Surface and Coatings Technology 206 (2012) 4872–4880.

[26] C. R. C. Lima, J. M. Guilemany, Adhesion improvements of Thermal Barrier Coatings with HVOF thermally sparyed bond coats, Surface and Coatings Technology 201 (2007) 4694–4701.

[27] R. Ghasemi, H. Vakilifard, Plasma-sprayed nanostructured YSZ thermal barrier coatings: Thermal insulation capability and adhesion strength, Ceramics International 43 (2017) 8556–8563.

[28] L. Wang, Q. Fan, Y. Liu, G. Li, H. Zhang, Q. Wang, F. Wang, Simulation of damage and failure processes of thermal barrier coatings subjected to a uniaxial tensile load, Materials and Design 86 (2015) 89–97.

[29] E. E. Balic, M. Hadad, P. P. Bandyopadhyay, J. Michler, Fundamentals of adhesion of thermal spray coatings: Adhesion of single splats, Acta Materialia 57 (2009) 5921–5926.

[30] R. R. Chromik, D. Goldbaum, J. M. Shockley, S. Yue, E. Irissou, J. G. Legoux, N. X. Randall, Modified ball bond shear test for determination of adhesion strength of cold spray splats, Surface and Coatings Technology 205 (2010) 1409–1414.

[31] S. Guetta, M. H. Berger, F. Borit, V. Guipont, M. Jeandin, M. Boustie, Y. Ichikawa, K. Sakaguchi, K. Ogawa, Influence of particle velocity on adhesion of cold-sprayed splats, Journal of Thermal Spray Technology 18(3) (2009) 331–342.

[32] K. Z. Troost, P. van der Sluis, D. J. Gravesteijn, Microscale elastic?strain determination by backscatter kikuchi diffraction in the scanning electron microscope, Applied Physics Letters 62 (1993) 1110–1112.

[33] A. J. Wilkinson, G. Meaden, D. J. Dingley, High resolution mapping of strains and rotations using electron backscatter diffraction, Materials Science and Technology 22(11) (2006) 1271–1278.

[34] A. J. Wilkinson, G. Meaden, D. J. Dingley, High-resolution elastic strain measurement from electron backscatter diffraction patterns: New levels of sensitivity, Ultramicroscopy 106 (2006) 307–313.

[35] J. F. Nye, Some geometrical relations in dislocated crystals, Acta metallurgica 1 (1953) 153–162.

[36] N. A. Fleck, G. M. Muller, M. F. Ashby, J. Hutchinson, Strain gradient plasticity: Theory and experiment, Acta Metall. Mater. 42 (1994) 475–487.

[37] A. Arsenlis, D. M. Parks, Crystallographic aspects of geometrically-necessary and statistically-stored dislocation density, Acta Materialia 47 (1999) 1597–1611.

[38] A. J. Wilkinson, D. Randman, Determination of elastic strain fields and geometrically necessary dislocation distributions near nanoindents using electron back scatter diffraction, Philosophical Magazine 90 (2010) 1159–1177.

[39] J. W. Kysar, Y. Saito, M. S. Oztop, D. Lee, W. T. Huh, Experimental lower bounds on geometrically necessary dislocation density, International Journal of Plasticity 26 (2010) 1097–1123.

[40] S. Xia, B.X.Zhou, W. Chen, W. Wang, Effects of strain and annealing processes on the distribution of $\sigma 3$ boundaries in a ni-based superalloy, Scripta Materialia 54 (2006) 2019–2022.

[41] Y. Wang, W.Z.Shao, L. Zhen, L. Yang, X. Zhang, Flow behavior and microstructures of superalloy 718 during high temperature deformation, Materials Science and Engineering A 497 (2008) 479–486.

[42] J. C. Zhao, V. Ravikumar, A. M. Beltran, Phase precipitation and phase stability in nimonic 263, Metallurgical and Materials Transactions A 32A (2001) 1271–1282.

[43] S. Saeidi, K. T. Voisey, D. G. McCartney, Mechanical properties and microstructure of vps and hvof conicraly coatings, Journal of Thermal Spray Technology 20 (2011) 1231–1243.

[44] S. Deshpande, S. Sampath, H. Zhang, Mechanisms of oxidation and its role in microstructural evolution of metmetal thermal spray coatings-case study for Ni-Al, Surface and Coatings Technology 200 (2006) 5395–5406.

[45] R. Koch, The intrinsic stress of polycrystalline and epitaxial thin metal films, Journal of Physics: Condensed Matter 6 (1994) 9519–9550.

[46] R. T. Tung, J. M. Gibson, D. C. Jacobson, J. M. Poate, Liquid phase growth of epitaxial ni and co suicides, Applied Physics Letters 43 (1983) 476–478.

[47] D. A. Porter, K. E. Easterling, M. Y. Sherif, Phase Solidification in Metals and Alloys, Third Edition, CRC Press, 2009.

[48] S. Wang, E. Tian, C. Lung, Surface energy of arbitrary crystal plane of bcc and fcc metals, Journal of Physics and Chemistry of Solids 61 (2000) 1295–1300.

[49] S. Sampath, H. Herman, Rapid solidification and microstructure development during plasma spray deposition, Journal of Thermal Spray Technology 5 (1996) 445–456.

[50] V. I. Vodovin, Misfit dislocations in epitaxial heterostructures: Mechanisms of generation and multiplication, Physica Status Solidi A: Applications and Materials Science 171 (1999) 239–250.

[51] A. E. Romanov, W. Pompe, G. Beltz, J. S. Speck, Modeling of threading dislocation density reduction in heteroepitaxial layers, Physica Status Solidi B: Basic Solid State Physics 198 (1996) 599–613.

[52] S. I. Rao, P. M. Hazzledine, Atomistic simulations of dislocation-interface interactions in the Cu-Ni multilayer system, Philosophical Magazine A 80 (2000) 2011–2040.

[53] C. Cui, Y. Gu, H. Harada, D. Ping, A. Sato, Phase stability and yield stress of ni-base superalloys containing high Co and Ti, Metallurgical and Materials Transactions A 37A (2006) 3183–3190.

[54] T. B. Britton, A. J. Wilkinson, High resolution electron backscatter diffraction measurement of elastic strain variations in the presence of large lattice rotations, Ultramicroscopy 114 (2012) 82–95.

[55] W. D. Nix, B. M. Clemens, Crystallite coalescence: A mechanism for intrinsic tensile stresses in thin films, Journal of Materials Research 14 (1999) 3467–3473.

[56] T. Patterson, A. Leon, B. Jayaraj, J. Liu, Y. H. Sohn, Thermal cyclic lifetime and oxidation behavior of air plasma sprayed conicraly bond coats for thermal barrier coatings, Surface and Coatings Technology 203 (2008) 437–441.

[57] K. Matoy, H. Schönherr, T. Detzel, T. Schöberl, R. Pippan, C. Motz, G. Dehm, A comparative micro-cantilever study of the mechanical behavior of silicon based passivation films, Thin Solid Films 518 (2009) 247–256.